INTERNATIONAL JOURNAL FOR NUMERICAL METHODS IN ENGINEERING
Int. J. Numer. Meth. Engng 2006; **68**:503–524
Published online 11 April 2006 in Wiley InterScience (www.interscience.wiley.com). DOI: 10.1002/nme.1713

Charge distribution on thin conducting nanotubes—reduced 3-D model

Hui Chen[‡] and Subrata Mukherjee[*, †]

Department of Theoretical and Applied Mechanics, Kimball Hall, Cornell University, Ithaca, NY 14853, U.S.A.

SUMMARY

The subject of this paper is the calculation of charge distribution on the surfaces of thin conducting nanotubes in electrostatic problems, by the boundary element method (BEM). A line model of a nanotube is proposed here. This model overcomes the problem of dealing with nearly singular matrices that occur when the standard BEM is applied to very thin features (objects or gaps). This new approach is also very efficient. Numerical results are presented for selected examples. Copyright © 2006 John Wiley & Sons, Ltd.

KEY WORDS: charge distribution; conducting nanotubes; boundary element method

1. INTRODUCTION

Microelectromechanical systems (MEMS) have demonstrated important applications in a wide variety of industries including mechanical and aerospace, medicine, communications, information technology, etc. Nanoelectromechanical systems (NEMS) are 'smaller' MEMS in the sense that they have submicron critical dimensions. Owing primarily to their small size, NEMS can offer very high sensitivities (e.g. force sensitivities at the attonewton level, mass sensitivities at a single molecule or even a single atom level, and charge sensitivities at the level of the charge on a single electron). In addition, they offer mechanical quality factors in the tens of thousands and fundamental frequencies in the microwave range [1, 2]. Fabrication of silicon nanotweezers [3] and nanoresonators [4] has been demonstrated recently. Carbon nanotubes have remarkable properties—they are very stiff, have low density, ultra-small cross-sections and can

*Correspondence to: Subrata Mukherjee, Department of Theoretical and Applied Mechanics, Kimball Hall, Cornell University, Ithaca, NY 14853, U.S.A.
†E-mail: sm85@cornell.edu
‡E-mail: hc267@cornell.edu

Contract/grant sponsor: National Science Foundation; contract/grant numbers: EEC-0303674, CMS-0508466

Received 11 October 2005
Revised 31 January 2006
Accepted 9 February 2006

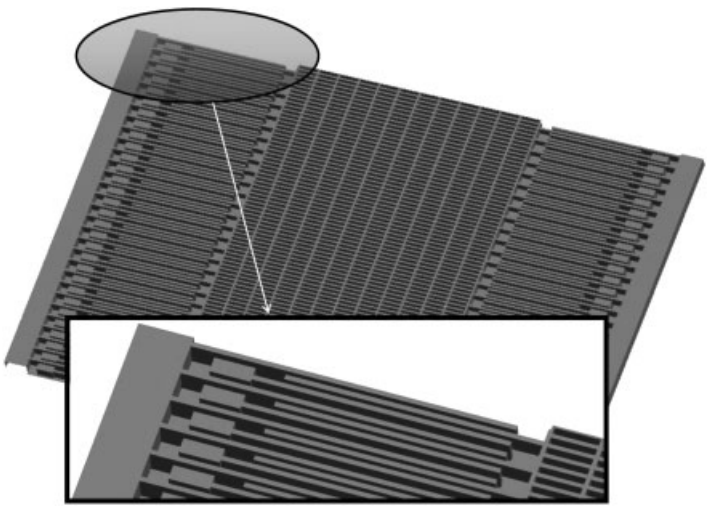

Figure 1. Parallel plate resonator: geometry and detail of the parallel plate fingers (from Reference [24]).

be defect free. They offer fascinating applications possibilities. Natural frequencies of tunable carbon nanotubes have been measured recently [5].

Numerical simulation of electrically actuated MEMS devices have been carried out for nearly fifteen years by using the boundary element method (BEM—see, e.g. References [6–10]) to model the exterior electric field and the finite element method (FEM—see, e.g. References [11–13]) to model deformation of the structure. The commercial software package MEMCAD [14], for example, uses the commercial FEM software package ABAQUS for mechanical analysis, together with a BEM code FastCap [15] for the electric field analysis. Other examples of such work are References [16–19]; as well as References [14, 20, 21] for dynamic analysis of MEMS. A very nice recent example of NEMS simulation is Reference [22]. This paper employs the classical electrostatic model for nano conductors and, depending upon their characteristic length, two different electrostatic models: semiclassical and quantum-mechanical, for semiconductors. A just published paper [23] addresses the problem of charge distribution on multiwalled nanotubes, with a classical electrostatics model, by employing a full three-dimensional (3-D) BEM approach.

The focus of this paper is the study of the charge distribution on thin *conducting* carbon nanotubes (CNTs). This requires BEM analysis of the electric field exterior to these thin conducting objects. In the context of MEMS with very thin beams or plates (see Figure 1), a convenient way to model such a problem is to assume plates with vanishing thickness and solve for the sum of the charges on the upper and lower surfaces of each plate [25]. The standard boundary integral equation (BIE) with a weakly singular kernel is used in Reference [25] and this approach works well for determining, for example, the capacitance of a parallel plate capacitor. For MEMS calculations, however, one must obtain the charge densities separately on the upper and lower surfaces of a plate since the traction at a surface point on a plate depends on the square of the charge density at that point. The gradient BIE is employed in Reference [26]

to obtain these charge densities separately. The formulation given in Reference [26] is a BEM scheme that is particularly well-suited for MEMS analysis of very thin plates—for $h/L \leqslant 0.001$—in terms of the length L (of a side of a square plate) and its thickness h. A similar approach has also been developed for MEMS with very thin beams [27]. Similar work has also been reported recently by Chuyan *et al.* [28] in the context of determining fringing fields and levitating forces for 2-D beam shaped conductors in MEMS combdrives. A fully coupled BEM/FEM MEMS calculation with very thin plates has just been completed [29]. See, also Reference [30] for an application of the thin plate idea for modelling damping forces on MEMS with thin plates.

It is important to cite related work on BEM modelling of thin bodies (other than in MEMS). Some important papers are References [31–37]. The research presented in Reference [31], in particular, has been a real inspiration for the present work.

As stated earlier, the focus of the present paper is applying the BEM to compute the charge densities on the surfaces of *conducting* carbon nanotubes. The classical electrostatic model, which assumes that all charges reside on the surface of the conductor and that the electric potential is constant inside and on the surface of the conductor, is employed here. Use of the classical electrostatic model requires justification in view of the fact that CNTs are nanoscale objects. This issue is very clearly discussed in Reference [22]. First, it is re-emphasized here that the region exterior to a CNT (rather than mechanical deformations of the CNT itself) is of interest in the present work. (Please see, for example, Reference [38] for recent work on modelling of mechanical deformation of CNTs). Second, it is of course well-known that CNTs can be conducting or semiconducting depending upon their chirality [22]. Attention is focussed in the present work, however, only on *conducting* carbon nanotubes for which the classical electrostatic model applies. Semiconducting nanotubes might require the employment of other electrostatic models such as semiclassical or quantum mechanical, depending on their (geometric) characteristic length [22].

The primary contribution of the present work, therefore, is the development of a line model of a nanotube in a 3-D region (called a reduced 3-D model). This model overcomes the problem of dealing with nearly singular matrices that occur when the standard BEM is applied to very thin gaps. It also greatly simplifies the BEM calculations and is computationally very efficient. Finally, the actual charge distribution on the entire surface of a CNT can be recovered *at a post-processing step*!

The present paper is organized as follows. BIEs are first presented for an infinite region containing one thin conducting nanotube and the (infinite) ground plane. The ground is modelled indirectly by adding a suitable image nanotube to the computational domain. This approach of modelling the ground plane is quite standard (see, e.g. References [23, 26, 27]). An alternate implicit ground model, using a modified Green function, is also presented in this paper. Next, several sections deal with evaluation of various integrals—singular and otherwise. Some of these evaluations are rather subtle and of critical importance for obtaining the numerical results presented in this paper. The next section deals with a region containing an arbitrary number of tubes, together with the ground plane. Each tube can be of arbitrary length and be oriented in an arbitrary direction in space. A numerical results section and a concluding remarks section complete the paper. Numerical results for the charge density on the surface of a CNT, from this reduced 3-D model, are compared with those from an analytical expression for a tube of infinite length [39, p. 159], a new analytical solution (25), (26), a full 3-D BEM model [23], and also a 2-D cross-section model.

2. BIEs IN SEMI-INFINITE REGION CONTAINING ONE THIN CONDUCTING NANOTUBE AND THE GROUND

2.1. Nanotube models

A carbon nanotube (CNT) is a thin hollow tube, of circular cross-section, as shown in Figure 2. This figure shows a straight tube, but a CNT can be bent.

2.2. Direct regular BIE for 3-D potential theory outside a doubly-connected body

Consider a 3-D prismatic doubly-connected conductor. Its cross-section is shown in Figure 3 and its two ends are denoted (together) as ∂B_E. The potential ϕ satisfies Laplace's equation in the 3-D region B outside the conductor.

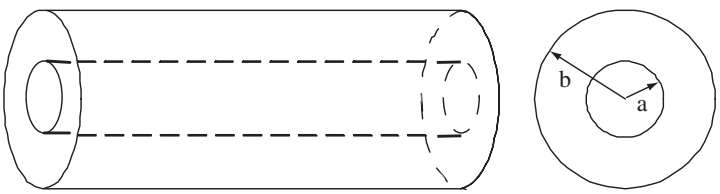

Figure 2. A carbon nanotube.

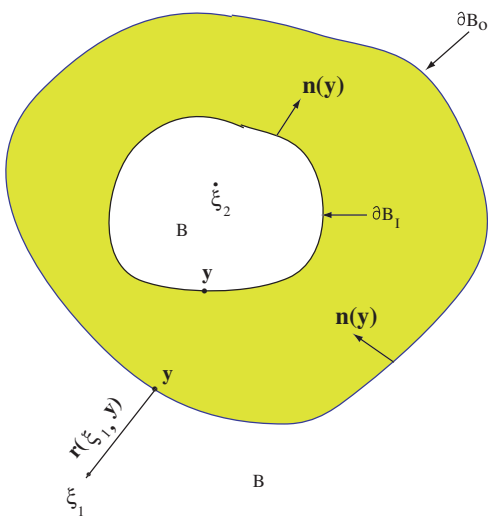

Figure 3. Cross-section of a prismatic doubly-connected conductor.

The direct regular BIE governing the potential ϕ for this problem is of the form [10]

$$\phi(\xi) = \int_{\partial B_0} \frac{\sigma(\mathbf{y})}{4\pi\varepsilon r(\xi,\mathbf{y})}\,\mathrm{d}s(\mathbf{y}) + \int_{\partial B_I} \frac{\sigma(\mathbf{y})}{4\pi\varepsilon r(\xi,\mathbf{y})}\,\mathrm{d}s(\mathbf{y}) + \int_{\partial B_0} \frac{\mathbf{r}(\xi,\mathbf{y})\cdot\mathbf{n}(\mathbf{y})\phi(\mathbf{y})}{4\pi r^3(\xi,\mathbf{y})}\,\mathrm{d}s(\mathbf{y}) + \int_{\partial B_I} \frac{\mathbf{r}(\xi,\mathbf{y})\cdot\mathbf{n}(\mathbf{y})\phi(\mathbf{y})}{4\pi r^3(\xi,\mathbf{y})}\,\mathrm{d}s(\mathbf{y}) + C + \int_{\partial B_E} \frac{\sigma(\mathbf{y})}{4\pi\varepsilon r(\xi,\mathbf{y})}\,\mathrm{d}s(\mathbf{y}) + \int_{\partial B_E} \frac{\mathbf{r}(\xi,\mathbf{y})\cdot\mathbf{n}(\mathbf{y})\phi(\mathbf{y})}{4\pi r^3(\xi,\mathbf{y})}\,\mathrm{d}s(\mathbf{y}), \quad \xi \in B \tag{1}$$

In (1), $\mathbf{r}(\xi,\mathbf{y})$ is the vector from a source point ξ to a field point $\mathbf{y}$, $r(\xi,\mathbf{y})$ is its magnitude, $\mathbf{n}(\mathbf{y})$ is the unit normal to the boundary of the conductor (pointing into the conductor) at $\mathbf{y}$, σ is the charge density, per unit area, on the conductor surface and ε is the dielectric constant of the medium outside the conductor. Also, $C = \phi_\infty$, the potential at infinity. Finally,

$$\sigma(\mathbf{x}) = \varepsilon\frac{\partial\phi}{\partial n}(\mathbf{x}) = \varepsilon\mathbf{n}(\mathbf{x})\cdot[\nabla_\xi\phi(\xi)]_{\xi=\mathbf{x}} \tag{2}$$

where $\mathbf{x}$ is a source point on the conductor surface.

Problems of interest in this work involve long thin conductors with a finite potential ϕ prescribed on the entire surface of a conductor including its ends. Also, the charge density σ is assumed to be finite over the entire surface. In view of this, the integrals over the ends (i.e. over ∂B_E) are neglected in (1).

The potential is a constant (call this value $\bar{\phi}$) at every point on the surface as well as inside a conductor. This fact leads to very significant simplification of Equation (1). Consider a Dirichlet problem for Laplace's equation in a simply-connected region with $\phi = A$ prescribed on its entire boundary ∂B_I. It is well known that the solution of this problem at all points inside this simply-connected region is also $\phi = A$. Thus, a hollow conductor with uniform potential has zero charge on its inside surface. Therefore, the second integral on the right-hand side of (1) vanishes since $\sigma(\mathbf{y}) = 0$ for $\mathbf{y} \in \partial B_I$. For a source point ξ_1 (outside the conductor) the third and fourth integrals on the right-hand side of (1) vanish since the solid angles subtended by ∂B_0 and ∂B_I at ξ_1 are zero. Also, the solid angles subtended by ∂B_0 and ∂B_I at ξ_2 are -4π and 4π; so that the third and fourth integrals on the right-hand side of (1) become $-\bar{\phi}$ and $\bar{\phi}$, respectively, for a source point ξ_2. Finally, only the first integral on the right-hand side of (1) survives for any source point $\xi \in B$.

2.3. BIEs for a CNT with the ground modelled with an image tube

This section presents BIEs for a single thin conducting nanotube with an infinite ground plane. The ground is modelled by adding on a suitable image nanotube in the computational domain (see Figures 4 and 5).

2.3.1. Regular BIE—source point approaching the nanotube axis s_1. For a source point $\xi \in B \to \mathbf{x} \in \hat{s}_1 \subset s_1$ (see Figures 4 and 5), one has

$$\phi(\mathbf{x}) = \int_{\partial\bar{B}_{N1}} \frac{q(\mathbf{y})}{4\pi\varepsilon r(\mathbf{x},\mathbf{y})}\,\mathrm{d}\ell(\mathbf{y}) + \int_{\tilde{s}_1} \frac{q(\mathbf{y})}{4\pi\varepsilon r(\mathbf{x},\mathbf{y})}\,\mathrm{d}\ell(\mathbf{y}) + C, \quad \mathbf{x} \in \hat{s}_1 \subset s_1 \tag{3}$$

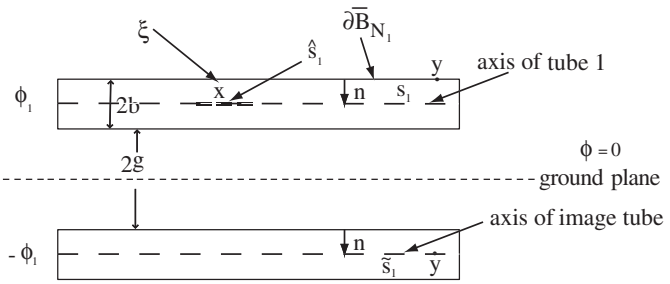

Figure 4. Nanotube with image.

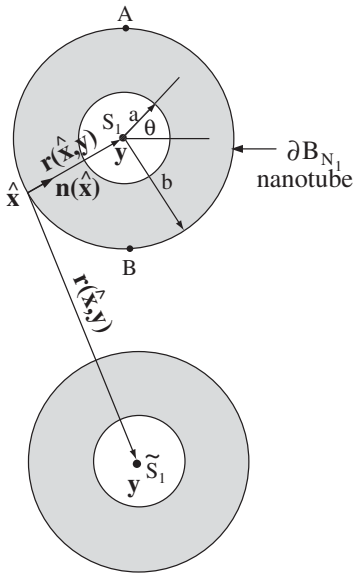

Figure 5. Nanotube cross-section with image.

with

$$q(\mathbf{y}) = \int_0^{2\pi} \sigma(y_3, b, \theta) b \, \mathrm{d}\theta, \quad y_3 \in s_1 \text{ or } \tilde{s}_1 \tag{4}$$

Here, σ is the charge density, per unit surface area, on the nanotube and q is the charge density, per unit length, on the nanotube axis s_1. The axial co-ordinate for a straight nanotube is y_3. For a bent nanotube, y_3 must be replaced by the arc length co-ordinate ℓ along the (bent) axis of the tube and the integration in (4) must be carried out on a planar cross-section of the tube that is normal to the local arc length direction.

It is first noted that the source point $\mathbf{x}$ in (3) lies inside rather than on the surface of a nanotube. The potential at any such point $\mathbf{x}$, however, is known (it is the same as on the

nanotube surface) and can be used as a 'boundary' condition. Also, both tubes are assumed to be very thin and a line model is used for each of them.

Equation (3) follows from (1) upon making use of the fact that the nanotube is very thin. Specifically, the starting point for the first integral on the right-hand side of (3) is the double integral

$$\int_{\partial \bar{B}_{N_1}} \mathrm{d}\ell(\mathbf{y}) \int_0^{2\pi} \frac{\sigma(\mathbf{y}) b \, \mathrm{d}\theta}{4\pi\varepsilon r(\mathbf{x}, \mathbf{y})} \tag{5}$$

where $\partial \bar{B}_{N_1}$ is a line on the nanotube surface ∂B_{N_1} which is parallel to the nanotube axis s_1. In view of (5), and the fact that $r(\mathbf{x}, \mathbf{y})$ in this case is, in fact, independent of $\mathbf{y}$ (and therefore of θ), the first term on the right-hand side of (3) is exact. The second integral on the right-hand side of (3) follows from the assumption that $g \gg b$ (where g is the gap between the nanotube and the ground and b in the nanotube radius (see Figures 4 and 5)). Therefore, one has $r(\mathbf{x}, \mathbf{y}) \gg b$ and it is assumed that r is independent of θ with the field point $\mathbf{y}$ moving on the boundary of a cross-section of the image nanotube. Next, $r(\mathbf{x}, \mathbf{y})$ is approximated to be the distance from $\mathbf{x} \in s_1$ and $\mathbf{y} \in \tilde{s}_1$. Exactly how large g has to be compared to b is a matter that needs further investigation. This matter is discussed later in this paper.

The first integral in (3) is nearly strongly singular and the second is regular. An evaluation procedure for the first integral is discussed in Section 2.5.

It is noted that in Figure 4, with the charge $q(\mathbf{y})$ at a point $\mathbf{y} \in s_1$, the charge is $-q(\mathbf{y})$ at a corresponding point on the axis of the image nanotube $\mathbf{y} \in \tilde{s}_1$. It is proved in Reference [27] that, for a two-dimensional (2-D) model of the thin beam problem, with potentials ϕ_1 and $-\phi_1$ on the two beams, one has

$$\phi_\infty = C = 0 \tag{6}$$

It is easy to show that the same arguments apply to the 3-D case as well. Therefore, $C = 0$ in (3).

Given ϕ, Equation (3) can be solved for $q(\mathbf{y})$ on s_1.

2.3.2. Gradient BIE—source point approaching the nanotube surface ∂B_{N_1}. Let $\boldsymbol{\xi} \to \hat{\mathbf{x}} \in \partial B_{N_1}$ (see Figure 5). Using (3) and (2), one can write

$$\sigma(\hat{\mathbf{x}}) = \int_{s_1 \cup \tilde{s}_1} \frac{\mathbf{r}(\hat{\mathbf{x}}, \mathbf{y}) \cdot \mathbf{n}(\hat{\mathbf{x}}) q(\mathbf{y})}{4\pi r^3(\hat{\mathbf{x}}, \mathbf{y})} \, \mathrm{d}\ell(\mathbf{y}), \quad \hat{\mathbf{x}} \in \partial B_{N_1} \tag{7}$$

With $q(\mathbf{y})$ known, (7) can be used, *as a post-processing step*, to find the charge density distribution $\sigma(\mathbf{x})$ on the outer surface of the nanotube with axis s_1.

Again, a line model is assumed for each of the nanotubes, i.e. the integrals on their surfaces are replaced by those on their axes.

The integral on s_1 in (7) is nearly hypersingular. Its evaluation is discussed in Section 2.5.2. The integral on $\tilde{s}_1$ is regular.

2.4. BIEs for a CNT with implicit modelling of the ground

This section presents alternate equations for the same physical situation as depicted in Section 2.3. A modified Green function is employed here.

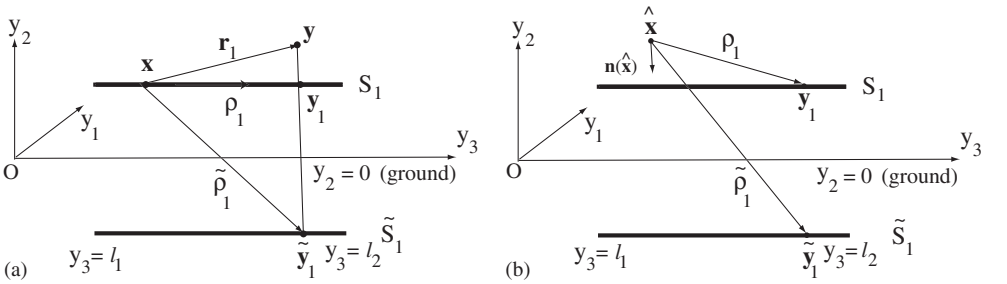

Figure 6. Modified Green's function approach: (a) regular BIE; and (b) gradient BIE.

2.4.1. Regular BIE—source point approaching the nanotube axis s_1. Please refer to Figure 6(a). Here, $\mathbf{y} \in \partial B_{N_1}$, $\mathbf{y}_1 \in s_1$ and $\tilde{\mathbf{y}}_1 \in \tilde{s}_1$. With $\mathbf{y}_1 : (y_1, y_2, y_3)$ and the ground at $y_2 = 0$, one has $\tilde{\mathbf{y}}_1 : (y_1, -y_2, y_3)$. (This is true even if the physical nanotube is bent.) Also, let

$$\mathbf{r}_1 = \mathbf{y} - \mathbf{x}, \quad \boldsymbol{\rho}_1 = \mathbf{y}_1 - \mathbf{x}, \quad \tilde{\boldsymbol{\rho}}_1 = \tilde{\mathbf{y}}_1 - \mathbf{x} \tag{8}$$

For a source point $\mathbf{x} \in \hat{s}_1 \subset s_1$, one has (see (3))

$$\phi(\mathbf{x}) = \int_{\partial \bar{B}_{N1}} \frac{q(\mathbf{y})}{4\pi\varepsilon r_1(\mathbf{x}, \mathbf{y})} \, \mathrm{d}\ell(\mathbf{y}) - \int_{\tilde{s}_1} \frac{q(\mathbf{y})}{4\pi\varepsilon \tilde{\rho}_1(\mathbf{x}, \tilde{\mathbf{y}}_1)} \, \mathrm{d}\ell(\tilde{\mathbf{y}}_1), \quad \mathbf{x} \in \hat{s}_1 \subset s_1 \tag{9}$$

Equation (9) can be written in more compact form as

$$\phi(\mathbf{x}) = \int_{\ell_1}^{\ell_2} \frac{q(\mathbf{y})}{4\pi\varepsilon} \left[\frac{1}{r_1} - \frac{1}{\tilde{\rho}_1} \right] \mathrm{d}\ell \tag{10}$$

It is noted that, on a straight nanotube, $\mathrm{d}\ell = \mathrm{d}y_3$.

2.4.2. Gradient BIE—source point approaching the nanotube surface ∂B_{N_1}. Referring to Figure 6(b), and with $\boldsymbol{\rho}_1 = \mathbf{y}_1 - \hat{\mathbf{x}}$, $\tilde{\boldsymbol{\rho}}_1 = \tilde{\mathbf{y}}_1 - \hat{\mathbf{x}}$, the equation corresponding to (7) is

$$\sigma(\hat{\mathbf{x}}) = \int_{\ell_1}^{\ell_2} \frac{q(\mathbf{y})}{4\pi} \left[\frac{\boldsymbol{\rho}_1}{\rho_1^3} - \frac{\tilde{\boldsymbol{\rho}}_1}{\tilde{\rho}_1^3} \right] \cdot \mathbf{n}(\hat{\mathbf{x}}) \, \mathrm{d}\ell, \quad \hat{\mathbf{x}} \in \partial B_{N_1} \tag{11}$$

2.5. Evaluation of singular integrals

2.5.1. First integral in (3). This nearly strongly singular integral is evaluated as follows (see Figure 7):

$$\int_{\partial \bar{B}_{N_1}} \frac{q(\mathbf{y})}{4\pi\varepsilon r(\mathbf{x}, \mathbf{y})} \, \mathrm{d}\ell(\mathbf{y}) = \int_{\partial \bar{B}_{N_1} - \partial \hat{\bar{B}}_{N_1}} \frac{q(\mathbf{y})}{4\pi\varepsilon r(\mathbf{x}, \mathbf{y})} \, \mathrm{d}\ell(\mathbf{y}) + \int_{\partial \hat{\bar{B}}_{N_1}} \frac{z}{r(\mathbf{x}, \mathbf{y})} \frac{[q(\mathbf{y}) - q(\hat{\mathbf{x}})]}{4\pi\varepsilon z} \, \mathrm{d}\ell(\mathbf{y})$$

$$+ \frac{q(\hat{\mathbf{x}})}{4\pi\varepsilon} \int_{-\hat{\ell}/2}^{\hat{\ell}/2} \frac{\mathrm{d}z}{\sqrt{z^2 + b^2}}, \quad \mathbf{x} \in \text{centre of } \hat{s} \tag{12}$$

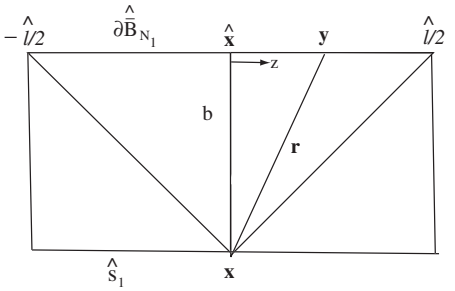

Figure 7. Evaluation of last integral in (12).

where the length of the nanotube segment $\hat{s}_1$ is $\hat{\ell}$. This segment is assumed to be straight and the last integral on the right-hand side of (12), which is nearly strongly singular, is evaluated analytically.

Please note that the field point $\mathbf{y}$ is placed on the outer surface ∂B_N of the nanotube while the source point $\mathbf{x}$ lies on its axis s_1. The quantity $z/r(\mathbf{x}, \mathbf{y})$ in the second integral on the right-hand side of (12) is $\mathcal{O}(1)$ and $\to 0$ as $\mathbf{y} \to \hat{\mathbf{x}}$. Therefore, the total integrand in this integral is regular. (See Reference [26] for the use of a similar idea for the evaluation of nearly weakly singular integrals).

Finally, it is assumed that $q(\mathbf{x}) = q(\hat{\mathbf{x}})$ in (12). The source point $\mathbf{x}$ is at the mid-point of $\hat{s}_1$ in the last integral on the right-hand side of (12) (see Figure 7). Please refer to Appendix A for the general situation where $\mathbf{x}$ is any point on $\hat{s}_1$.

2.5.2. Integral on s_1 in (7). This nearly hypersingular integral is evaluated as follows:

$$
\begin{aligned}
&\int_{s_1} \frac{\mathbf{r}(\hat{\mathbf{x}}, \mathbf{y}) \cdot \mathbf{n}(\hat{\mathbf{x}}) q(\mathbf{y})}{4\pi r^3(\hat{\mathbf{x}}, \mathbf{y})} \, \mathrm{d}\ell(\mathbf{y}) \\
&= \int_{s_1 - \hat{s}_1} \frac{\mathbf{r}(\hat{\mathbf{x}}, \mathbf{y}) \cdot \mathbf{n}(\hat{\mathbf{x}}) q(\mathbf{y})}{4\pi r^3(\hat{\mathbf{x}}, \mathbf{y})} \, \mathrm{d}\ell(\mathbf{y}) \\
&\quad + \int_{\hat{s}_1} \frac{\mathbf{r}(\hat{\mathbf{x}}, \mathbf{y}) \cdot \mathbf{n}(\hat{\mathbf{x}}) [q(\mathbf{y}) - q(\bar{\mathbf{x}}) - q'(\bar{\mathbf{x}})(\mathbf{y} - \bar{\mathbf{x}})]}{4\pi r^3(\hat{\mathbf{x}}, \mathbf{y})} \, \mathrm{d}\ell(\mathbf{y}) \\
&\quad + q(\bar{\mathbf{x}}) \int_{\hat{s}_1} \frac{\mathbf{r}(\hat{\mathbf{x}}, \mathbf{y}) \cdot \mathbf{n}(\hat{\mathbf{x}})}{4\pi r^3(\hat{\mathbf{x}}, \mathbf{y})} \, \mathrm{d}\ell(\mathbf{y}) \\
&\quad + q'(\bar{\mathbf{x}}) \int_{\hat{s}_1} \frac{\mathbf{r}(\hat{\mathbf{x}}, \mathbf{y}) \cdot \mathbf{n}(\hat{\mathbf{x}})(\mathbf{y} - \bar{\mathbf{x}})}{4\pi r^3(\hat{\mathbf{x}}, \mathbf{y})} \, \mathrm{d}\ell(\mathbf{y}), \quad \hat{\mathbf{x}} \in \partial \hat{B}_{N_1} \subset \partial B_{N_1}
\end{aligned}
\tag{13}
$$

where $\bar{\mathbf{x}} \in \hat{s}_1$ is closest to $\hat{\mathbf{x}} \in \partial B_{N_1}$ (see Figure 8). Also, $\hat{\mathbf{x}}$ is at the mid-point of the segment $\partial \hat{B}_{N_1}$ of ∂B_{N_1}. This is sufficient since (7) is a post-processing step.

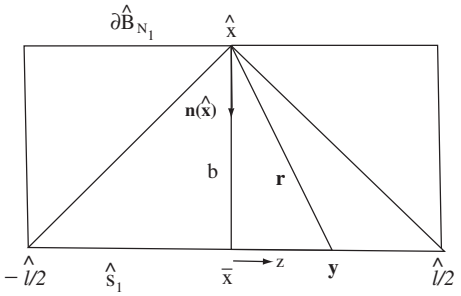

Figure 8. Evaluation of third integral in (13).

Referring to Figure 8, for a piecewise quadratic approximation for $q(\mathbf{y})$, the second integral on the right-hand side of (13) (using the Taylor series for $q(\mathbf{y})$ about $\bar{\mathbf{x}}$) becomes

$$\frac{q''(\bar{\mathbf{x}})}{8\pi}\int_{-\hat{\ell}/2}^{\hat{\ell}/2}\frac{bz^2\,\mathrm{d}z}{(z^2+b^2)^{3/2}} \tag{14}$$

This integral can be evaluated analytically.

Again referring to Figure 8, the third integral on the right-hand side of (13) becomes

$$q(\bar{\mathbf{x}})\int_{\hat{s}_1}\frac{\mathbf{r}(\hat{\mathbf{x}},\mathbf{y})\cdot\mathbf{n}(\hat{\mathbf{x}})}{4\pi r^3(\hat{\mathbf{x}},\mathbf{y})}\,\mathrm{d}\ell(\mathbf{y})=\frac{q(\bar{\mathbf{x}})}{4\pi}\int_{-\hat{\ell}/2}^{\hat{\ell}/2}\frac{b\,\mathrm{d}z}{(z^2+b^2)^{3/2}} \tag{15}$$

This integral can be evaluated analytically. The last integral on the right-hand side of (13) is

$$q'(\bar{\mathbf{x}})\int_{\hat{s}_1}\frac{\mathbf{r}(\hat{\mathbf{x}},\mathbf{y})\cdot\mathbf{n}(\hat{\mathbf{x}})(\mathbf{y}-\bar{\mathbf{x}})}{4\pi r^3(\hat{\mathbf{x}},\mathbf{y})}\,\mathrm{d}\ell(\mathbf{y})=\frac{q'(\bar{\mathbf{x}})}{4\pi}\int_{-\hat{\ell}/2}^{\hat{\ell}/2}\frac{bz\,\mathrm{d}z}{(z^2+b^2)^{3/2}}=0 \tag{16}$$

Finally, (13) has the simple form

$$\begin{aligned}\int_{s_1}\frac{\mathbf{r}(\hat{\mathbf{x}},\mathbf{y})\cdot\mathbf{n}(\hat{\mathbf{x}})q(\mathbf{y})}{4\pi r^3(\hat{\mathbf{x}},\mathbf{y})}\,\mathrm{d}\ell(\mathbf{y})&=\int_{s_1-\hat{s}_1}\frac{bq(\mathbf{y})}{4\pi r^3(\hat{\mathbf{x}},\mathbf{y})}\,\mathrm{d}\ell(\mathbf{y})+\frac{q''(\bar{\mathbf{x}})}{8\pi}\int_{-\hat{\ell}/2}^{\hat{\ell}/2}\frac{bz^2\,\mathrm{d}z}{(z^2+b^2)^{3/2}}\\&\quad+\frac{q(\bar{\mathbf{x}})}{4\pi}\int_{-\hat{\ell}/2}^{\hat{\ell}/2}\frac{b\,\mathrm{d}z}{(z^2+b^2)^{3/2}},\quad \hat{\mathbf{x}}\in\partial\hat{B}_{N_1}\subset\partial B_{N_1}\end{aligned} \tag{17}$$

It is easy to observe from (7) and (17) that, for a single nanotube without the ground, $\sigma(\hat{\mathbf{x}})$, on any cross-section of a nanotube, is, as expected, axisymmetric.

For the numerical calculations, $\hat{\ell}$ in Figures 7 and 8 is taken to be the length of a boundary element.

2.6. Verification for one straight very long nanotube without the ground

Consider a very long thin nanotube without the ground. The nanotube is at a constant potential with $\phi_\infty = 0$. Assuming uniform charge distribution along the length of the tube, i.e. $q(\mathbf{y}) = q(\bar{\mathbf{x}})$, Equations (7) and (17) yield

$$\sigma(\hat{\mathbf{x}}) = \frac{q(\bar{\mathbf{x}})}{4\pi} \int_{-\infty}^{\infty} \frac{b\,\mathrm{d}z}{(z^2 + b^2)^{3/2}} = \frac{q(\bar{\mathbf{x}})}{2b\pi} \tag{18}$$

Equation (18) says that, as expected, the charge distribution on the outer boundary of any cross-section of such a nanotube is axisymmetric and $2b\pi\sigma(\hat{\mathbf{x}}) = q(\bar{\mathbf{x}})$.

3. BIEs FOR *N* THIN CONDUCTING NANOTUBES AND IMPLICIT MODELLING OF THE GROUND

Consider the case with N conducting nanotubes, with arbitrary lengths and orientations, and the ground with zero potential. (Figure 9 shows an example with two nanotubes.)

3.1. Regular BIEs for N tubes

Please refer to Figure 6(a). With $\mathbf{y} \in \partial B_{N_m}$, $\mathbf{y}_k \in s_k$, $\tilde{\mathbf{y}}_k \in \tilde{s}_k$, define, in an analogous manner

$$\mathbf{r}_m = \mathbf{y} - \mathbf{x}_m, \quad \boldsymbol{\rho}_k = \mathbf{y}_k - \mathbf{x}_m, \quad \tilde{\boldsymbol{\rho}}_k = \tilde{\mathbf{y}}_k - \mathbf{x}_m \tag{19}$$

The equation corresponding to (10), with $\mathbf{x}_m \in s_m$, is

$$\phi_m = \int_{\ell_{m_1}}^{\ell_{m_2}} \frac{q_m}{4\pi\varepsilon} \left[\frac{1}{r_m} - \frac{1}{\tilde{\rho}_m}\right] \mathrm{d}\ell + \sum_{k=1,\,k\neq m}^{N} \int_{\ell_{k_1}}^{\ell_{k_2}} \frac{q_k}{4\pi\varepsilon} \left[\frac{1}{\rho_k} - \frac{1}{\tilde{\rho}_k}\right] \mathrm{d}\ell, \quad m = 1, 2, \ldots, N \tag{20}$$

There is no sum over m in the first integral in (20). Given ϕ_m, $m = 1, 2, \ldots, N$, Equation (20) can be solved for $q(\mathbf{y})$ on s_k, $k = 1, 2, \ldots, N$.

3.2. Gradient BIEs for N tubes

Please refer to Figure 6(b). With $\hat{\mathbf{x}}_m \in \partial B_{N_m}$, define, in an analogous manner

$$\boldsymbol{\rho}_k = \mathbf{y}_k - \hat{\mathbf{x}}_m, \quad \tilde{\boldsymbol{\rho}}_k = \tilde{\mathbf{y}}_k - \hat{\mathbf{x}}_m \tag{21}$$

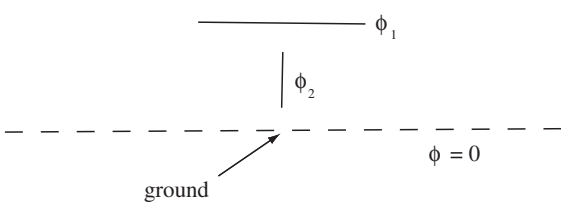

Figure 9. Two nanotubes with ground.

This time, the equation corresponding to (11) is

$$\sigma(\hat{\mathbf{x}}_m) = \int_{\ell_{m_1}}^{\ell_{m_2}} \frac{q_m}{4\pi}\left[\frac{\boldsymbol{\rho}_m}{\rho_m^3} - \frac{\tilde{\boldsymbol{\rho}}_m}{\tilde{\rho}_m^3}\right]\cdot \mathbf{n}(\hat{\mathbf{x}}_m)\,\mathrm{d}\ell$$

$$+ \sum_{k=1,\,k\neq m}^{N} \int_{\ell_{k_1}}^{\ell_{k_2}} \frac{q_k}{4\pi}\left[\frac{\boldsymbol{\rho}_k}{\rho_k^3} - \frac{\hat{\boldsymbol{\rho}}_k}{\hat{\rho}_k^3}\right]\cdot \mathbf{n}(\hat{\mathbf{x}}_m)\,\mathrm{d}\ell, \quad m = 1, 2, \ldots, N \tag{22}$$

There is no sum over m in the first integral in (22).

4. RESULTS

4.1. Analytical solutions for sample problems

Analytical solutions for q and σ, for two infinite conductive parallel (cylindrical) tubes with potentials ϕ and $-\phi$, are given below. (See Figures 10 and 4 which show two parallel finite tubes.)

For this case, one has [23, 39]

$$q = \frac{2\pi\varepsilon\phi}{\cosh^{-1}(1 + g/b)} \tag{23}$$

Referring to Figures 5 and 10, analytical solutions can be obtained for the charge densities $\sigma(A)$ and $\sigma(B)$. The points A and B lie on the middle cross-section of the (infinite) upper tube at $\theta = \pi/2$ and $\theta = 3\pi/2$, respectively.

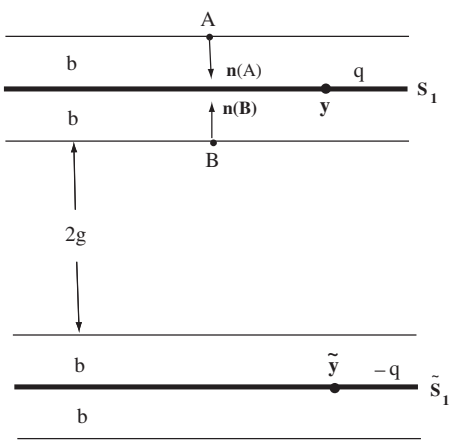

Figure 10. Two parallel nanotubes of infinite length.

Applying Equation (7), one gets

$$\sigma(A) = \int_{s_1} \frac{\mathbf{r}(\mathbf{A}, \mathbf{y}) \cdot \mathbf{n}(\mathbf{A}) q(\mathbf{y})}{4\pi r^3(A, \mathbf{y})} \, \mathrm{d}\ell(\mathbf{y}) - \int_{\tilde{s}_1} \frac{\mathbf{r}(\mathbf{A}, \mathbf{y}) \cdot \mathbf{n}(\mathbf{A}) q(\mathbf{y})}{4\pi r^3(A, \mathbf{y})} \, \mathrm{d}\ell(\mathbf{y}) \tag{24}$$

With q constant on an infinite tube (its value is given by (23)), using Figure 10, one has

$$\begin{aligned} \sigma(A) &= \frac{q}{4\pi} \int_{-\infty}^{\infty} \frac{b \, \mathrm{d}z}{(z^2 + b^2)^{3/2}} - \frac{q}{4\pi} \int_{-\infty}^{\infty} \frac{(2g + 3b) \, \mathrm{d}z}{[z^2 + (2g + 3b)^2]^{3/2}} \\ &= \frac{q}{2\pi b} - \frac{q}{2\pi} \left[\frac{1}{2g + 3b} \right] = \frac{q}{\pi b} \left[\frac{g + b}{2g + 3b} \right] \end{aligned} \tag{25}$$

Using a similar procedure, and noting that $\mathbf{r}(\mathbf{B}, \tilde{\mathbf{y}}) \cdot \mathbf{n}(\mathbf{B}) = -(2g + b)$ for $\tilde{\mathbf{y}} \in \tilde{s}_1$, one gets

$$\sigma(B) = \frac{q}{\pi b} \left[\frac{g + b}{2g + b} \right] \tag{26}$$

4.2. Numerical results for two parallel tubes in Figure 4

Numerical results are presented in this section for two parallel tubes of finite length (i.e. a nanotube with its image in order to model the ground plane). These results are then compared with the analytical solutions for infinite tubes that are presented in Section 4.1.

4.2.1. Material and geometrical parameters. The nominal values of the geometrical parameters are $\ell_N = 3000$ nm, $b = 1$ nm and $g = 500$ nm. Also, $\varepsilon = 8.854 \times 10^{-12}$ F/m and $\phi_1 = 1$ V and $\tilde{\phi}_1 = -1$ V, respectively. Of course, it is noted that such large voltages would be extremely hazardous to the health of CNTs. These numbers are chosen for illustrative purposes only. For practical applications, the results of these linear problems can be immediately scaled down to accommodate much lower applied voltages.

4.2.2. Verification of computer code. One-dimensional quadratic boundary elements are used to discretize each nanotube. The first and last boundary elements on a nanotube are non-conforming ones (with $\eta_1 = -0.5$, $\eta_2 = 0$, $\eta_3 = 1.0$; and $\eta_1 = -1.0$, $\eta_2 = 0$, $\eta_3 = 0.5$, respectively), to allow for singularities in q at the two ends of the nanotube. The rest of the elements are the usual quadratic conforming ones. Numerical results for q_0 (at the centre of the top tube), for nominal values of the parameters, for different numbers of elements on each nanotube, are shown in Table I. The analytical solution for q, for a pair of infinitely long tubes, from (23), is 8.051 pC/m. The difference, for 201 elements, is 1.25%.

4.2.3. Parameter study. Key dimensionless parameters in this problem are ℓ_N/b, ℓ_N/g and g/b. It is important to study the validity of the reduced 3-D BEM model for various values of these ratios. For example, the ratio ℓ_N/b must be large enough for this 'thin tube' model to work. Also, the reduced 3-D model will clearly break down for $g/b \approx 1$.

Results for varying, in turn, b, ℓ_N and g, keeping the other parameters at their nominal values, appear in Tables II, III and IV, respectively. Table II shows that the values of q_0 agree

Table I. Charge density q_0 at the centre of the upper nanotube as a function number of elements on the nanotube. $\ell_N = 3000$ nm, $b = 1$ nm, $g = 500$ nm. Two nanotube model with $\phi_1 = 1$ V, $\tilde{\phi}_1 = -1$ V and $\varepsilon = 8.854 \times 10^{-12}$ F/m.

Number of elements	q_0 at centre (pC/m)
11	8.1526
25	8.1523
51	8.1521
101	8.1520
201	8.1519

Table II. Charge density q_0 at the centre of the upper nanotube as a function of b with $\ell_N = 3000$ nm and $g = 500$ nm. Two nanotube model with $\phi_1 = 1$ V, $\tilde{\phi}_1 = -1$ V and $\varepsilon = 8.854 \times 10^{-12}$ F/m. The result from a full 3-D BEM model [23], for $b = 20$ nm, is $q_0 = 14.098$ pC/m.

	q_0 (pC/m)		
b (nm)	Computed	Exact for $\ell_N \to \infty$	Difference (%)
20	14.37	14.08	2.06
7.5	11.53	11.34	1.68
3	9.70	9.57	1.36
1	8.15	8.051	1.23

Table III. Charge density q_0 at the centre of the upper nanotube as a function of ℓ_N with $b = 1$ nm and $g = 500$ nm. Two nanotube model with $\phi_1 = 1$ V, $\tilde{\phi}_1 = -1$ V and $\varepsilon = 8.854 \times 10^{-12}$ F/m.

	q_0 (pC/m)		
ℓ_N (nm)	Computed	Exact for $\ell_N \to \infty$	Difference (%)
1000	8.59	8.051	6.65
1500	8.35	8.051	3.71
2000	8.24	8.051	2.34
3000	8.15	8.051	1.23

quite well with the analytical solution for an infinitely long tube for all cases. The complete numerical solution for $q(\mathbf{x})$, from the reduced 3-D model, however, exhibits oscillations at the two ends of the tube, for $b = 20$ nm and for $b = 7.5$ nm, as shown in Figure 11(a) and (b), respectively; while the solution for $b = 3$ nm and for $b = 1$ nm have the correct profile. It appears that the reduced 3-D model works best for $\ell_N/d \geqslant 500$ (here $d = 2b$ is the diameter of the tube). The model can also be used for smaller aspect ratios (e.g. $\ell_N/d \approx 100$) if one is only interested in the value of q_0. Finally, it is possible that inclusion of singular elements at the ends of a tube might damp out the oscillations in Figure 11(a) and (b). This investigation is planned for the future.

Table IV. Charge density q_0 at the centre of the upper nanotube as a function of g with $b = 1$ nm and $\ell_N = 3000$ nm. Two nanotube model with $\phi_1 = 1$ V, $\tilde{\phi}_1 = -1$ V and $\varepsilon = 8.854 \times 10^{-12}$ F/m.

	q_0 (pC/m)		
g (nm)	Computed	Exact for $\ell_N \to \infty$	Difference (%)
500	8.15	8.051	1.23
100	10.49	10.48	0.1
25	14.08	14.08	0
5	22.38	22.45	0.31

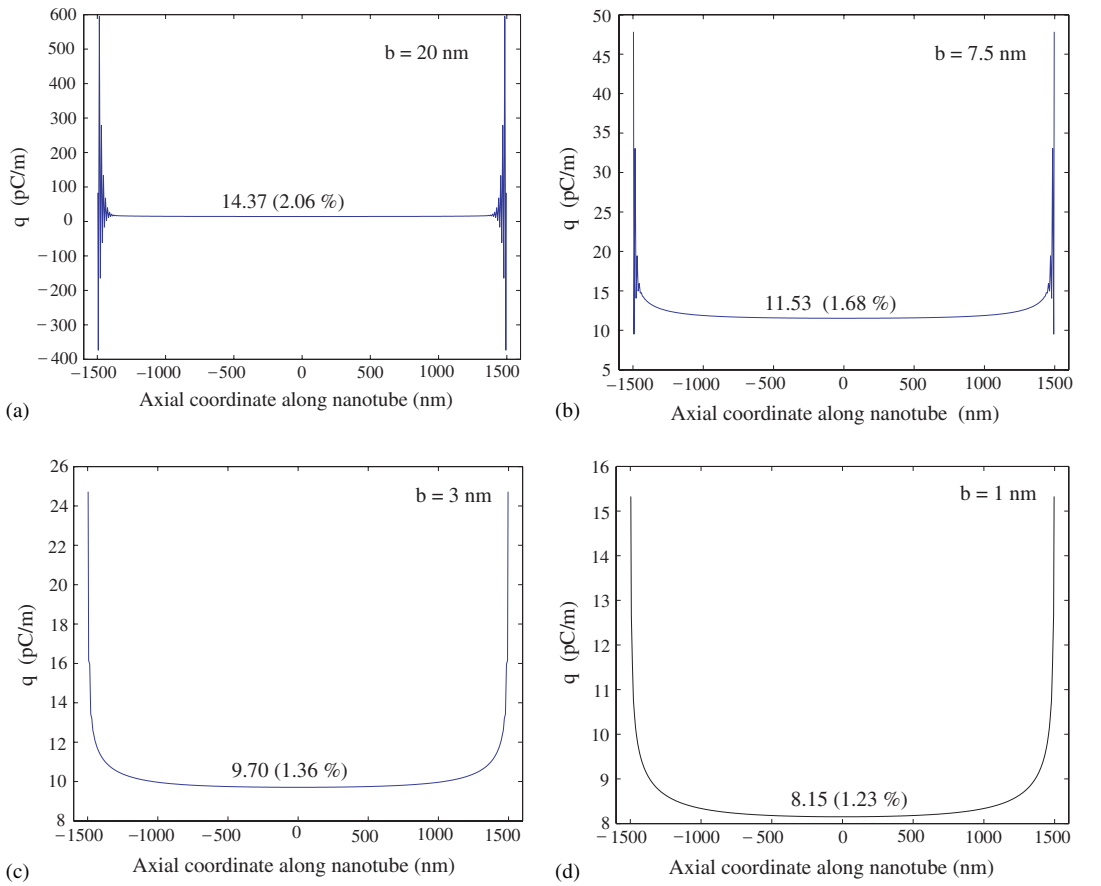

Figure 11. Charge density q per unit length along nanotube for different values of b, with $\ell_N = 3000$ nm and $g = 500$ nm. Two nanotube model with $\phi_1 = 1$ V, $\tilde{\phi}_1 = -1$ V and $\varepsilon = 8.854 \times 10^{-12}$ F/m (201 quadratic elements along each nanotube).

An interesting observation is made next regarding Table III. There is a difference of 6.65% between the result from the reduced 3-D model for $\ell_N/g = 2$ and the analytical solution for an infinitely long tube (23). This time, the solution (23) is not very accurate since the ratio ℓ_N/g is not large enough. This fact is also apparent from Figure 4 of Reference [23] which shows results from a full 3-D BEM model with $b = 20$ nm for various values of ℓ_N/g. There, also, the numerical solution is somewhat larger than the result from (23) for $\ell_N/g = 2$. The reduced 3-D model solution approaches the analytical solution (23) as ℓ_N/g increases to 6 in Table III. The same trend is observed in Figure 4 of Reference [23].

Finally, Table IV shows that the reduced 3-D model performs very well for $g/d \geqslant 2.5$. This is quite encouraging. The reduced 3-D model is expected to break down as $g \to 2b$.

It is noted that the results in Tables II–IV are obtained with 201 boundary elements on a nanotube.

4.2.4. Calculation of charge density σ on the surface of a nanotube. Figure 12 shows polar plots for $\sigma(\theta)$ on the central cross-section of the upper nanotube. The left column in this figure shows numerical results from the gradient BIE (7) for various values of g. The right column shows results from a 2-D cross-section model, which is a standard 2-D BIE calculation for the two-tube configuration shown in Figure 5. The numerical results for σ_A and σ_B, in the first column, agree with the analytical solutions (25), (26) up to 4 significant figures! As expected, the results from the reduced 3-D and the 2-D cross-section models agree well for large gap ($g/b = 500$) when the nanotubes hardly interact and the charge distribution is nearly axisymmetric around the tube. As g/b becomes smaller, however, anisotropy in $\sigma(\theta)$ sets in as expected, and it is observed that the 2-D cross-section model incorrectly intensifies the interaction between the tubes, and consequent anisotropy of $\sigma(\theta)$, because the 3-D interaction between the nanotubes is not modelled correctly by this greatly simplified model. It is interesting to note, however, that the 2-D cross-section model yields excellent values of q (using (4) to integrate the numerically obtained $\sigma(\theta)$ around the tube), even for $g/d = 2.5$, in spite of the fact that $\sigma(\theta)$ itself is not correct in this case.

4.3. Numerical results for three tubes and the ground

This example has three tubes—X, Y and Z tubes, arranged as shown in Figure 13, and the ground. The tubes are arranged such that, looking from the top, the X and Y tubes form a cross and the Z tube stands directly above it. The lengths of the tubes are ℓ_{N_k}, their potentials are ϕ_k and the gaps are g_k; $k = 1, 2, 3$. Each has radius $b = 1$ nm and $\varepsilon = 8.854 \times 10^{-12}$ F/m. Gaps are always measured from the outer surfaces of the tubes. In this example, $\ell_{N_1} = \ell_{N_2} = \ell_{N_3} = 3000$nm, $g_1 = g_2 = g_3 = 5$ nm and $\phi_1 = 1$, $\phi_2 = 2$, $\phi_3 = 3$ V, respectively.

Numerical results for the charge distributions along the X, Y and Z tubes, together with that on an isolated Z tube (i.e. the Z tube and the ground in the same positions as in Figure 13 without the X and Y tubes), appear in Figure 14. The 'asymptotic' values of charge shown in Figure 14(a) and (b) are the numerical values of q obtained at axial co-ordinates $= \pm 1001.1$ nm on the X and Y tubes, respectively; together with their percentage differences from the exact solution at the centre of a corresponding isolated infinite tube from (23). As expected, these values are very close. (Note that the gap g in (23) is 5 nm for the X and 12 nm for the Y tube, respectively.)

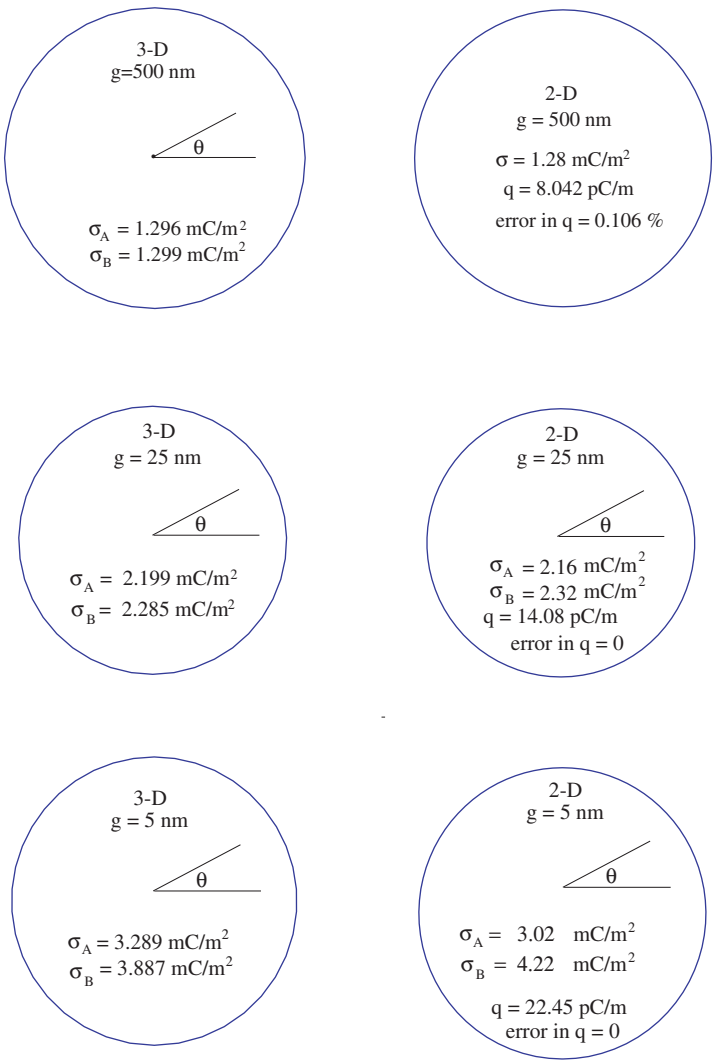

Figure 12. Polar plots of charge density per unit area around nanotube for different values of g with $\ell_N = 3000$ nm and $b = 1$ nm. Two nanotube model with $\phi_1 = 1$ V, $\tilde{\phi}_1 = -1$ V and $\varepsilon = 8.854 \times 10^{-12}$ F/m. Left column—reduced 3-D; right column—2-D cross-section model. Reduced 3-D numerical results for σ_A and σ_B agree with analytical solutions (25), (26) up to 4 significant figures. Points A and B are shown in Figure 5—they are located on the mid cross-section of the upper tube at $\theta = \pi/2$ and $\theta = 3\pi/2$, respectively.

Some interesting observations regarding Figure 14 are made below. Following a heat conduction analogy, it is known that positive charge corresponds to heat outflow and negative charge corresponds to heat inflow. Referring to Figure 14(a) and (b) (see, also, Figure 13), the centre

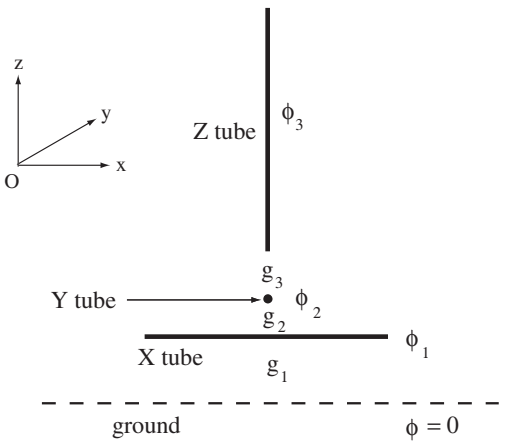

Figure 13. Configuration with three tubes.

of the X tube gains heat from the other two tubes, thereby significantly lowering its value of q there compared to its value on an isolated X tube. The centre of the Y tube, however, loses heat to the X tube and gains heat from the Z tube. The net result is a gain in heat since the incoming heat from the Z tube is 'more focussed' than the outgoing heat to the X tube. Therefore, the value of q at the centre of the Y tube also decreases compared to its value on an isolated Y tube. It is further observed that, as expected, the net percentage drop in the value of q at its centre is much less for the Y tube compared to that for the X tube.

Some observations are now made regarding Figure 14(c) and (d). Figure 14(d) shows that, for the isolated Z tube, both ends lose heat, but the lower end loses much more heat than the upper one since it is much closer to the ground. In Figure 14(c), the lower end of the Z tube loses less heat (because of the presence of the X and Y tubes) than when it is isolated, but the upper end is far from the lower one and is hardly affected by the presence of the X and Y tubes. (The numerical values of q are 42.395 and 42.429 pC/m, respectively, at the upper end of the Z tube in Figure 14(c) and (d).)

It is noted here that the values of q are, in fact, singular at each end of a tube. Singular boundary elements are needed to pick up these singularities, and such elements have not yet been included in these calculations. Nevertheless, the numerical values obtained at the ends of a tube, in this work, are expected to reflect the strengths of these singularities.

5. CONCLUDING REMARKS

- An efficient method (a reduced 3-D model) is presented in this paper for the calculation of charges on the surfaces of thin conducting nanotubes. The charge per unit length q is computed first, followed by the determination of σ, the pointwise charge per unit area on a tube surface, at a post-processing step. The first step (determination of q) is just a 1-D BEM calculation! This method works best for sufficiently thin tubes ($\ell_N/d \geqslant 500$) that can be near but not too close to each other ($g/d \geqslant 2.5$).

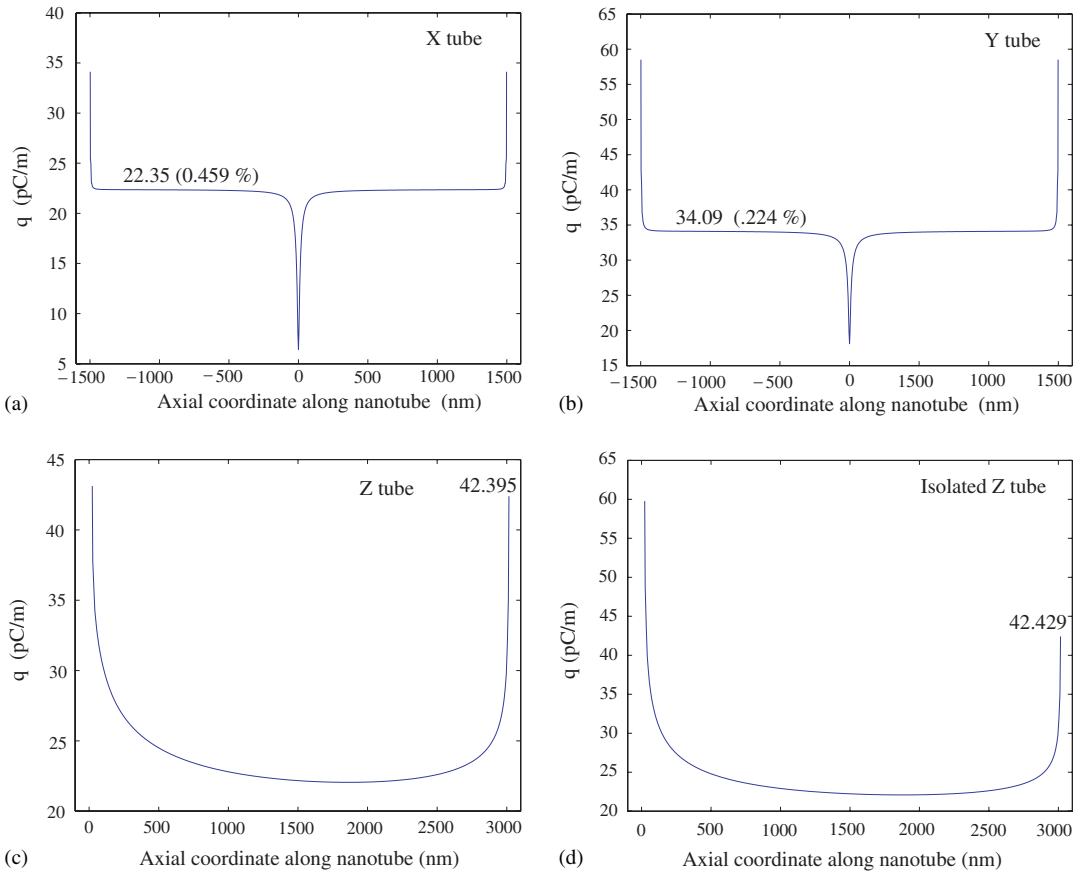

Figure 14. Charge density q per unit length along nanotubes X, Y and Z, together with that on an isolated Z tube, for the 3 tube problem. $b = 1$ nm, $\ell_{N_1} = \ell_{N_2} = \ell_{N_3} = 3000$ nm, $g_1 = g_2 = g_3 = 5$ nm, $\phi_1 = 1$, $\phi_2 = 2$, $\phi_3 = 3$ V, and $\varepsilon = 8.854 \times 10^{-12}$ F/m (451, 451 and 201 quadratic elements along X, Y and Z tubes, respectively).

- The numerical results are checked against analytical solutions whenever possible. (A new analytical result, Equations (25), (26), is derived in this work.) The performance of this reduced 3-D model is uniformly excellent.
- An elegant approach is presented here for solving a problem with N nanotubes, based on modified Green functions.
- Plans for future work:
  - — Study of semi-conducting nanotubes by employing a semi-classical model (Laplace/Poisson's equation [22]).
  - — Study of large problems (with many nanotubes) by the BEM accelerated by the Fast Multipole Method (FMM [40, 41]).

— Modelling of coupled elastic–electrostatic problems (see, e.g. Reference [29] for analogous MEMS problems).
— Dynamics problems including damping (see, e.g. Reference [30] for modelling of fluid damping forces in analogous MEMS problems).
— Applying the same idea to study charge distribution on narrow conducting beams in MEMS. A narrow beam is one with, say, a rectangular cross-section with both its width and height much less than its length.

APPENDIX A: INTEGRALS IN EQUATION (12)

The computer implementation in this paper uses 1-D quadratic elements, of which the first and last ones on a tube are non-conforming ones (with $\eta_1 = -0.5$, $\eta_2 = 0$, $\eta_3 = 1$ and $\eta_1 = -1$, $\eta_2 = 0$, $\eta_3 = 0.5$, respectively), to allow for singularities in q at the start of the first and at the end of the last element. The rest of the elements are the usual quadratic conforming ones. In view of this, three cases for the placement of a source point must be considered.

1. The source point $\mathbf{x}$ lies at the centre of an element. In this case, $\hat{s}_1$ is that singular element. This case has been discussed in the body of the paper (please see the last integral on the right-hand side of (12)).
2. The source point $\mathbf{x}$ lies at an arbitrary point inside an element. Again, $\hat{s}_1$ is that singular element.
   Let the local co-ordinate of the source point $\mathbf{x}$ on $\hat{s}_1$, with respect to the mid-point O of $\hat{s}_1$, be $\alpha\hat{\ell}/2$, with $\alpha \in (-1, 1)$ (Figure A1). The local co-ordinate z is measured from $\mathbf{x}$. Now, the last integral in (12) is

$$\frac{q(\mathbf{x})}{4\pi\varepsilon} \int_{-(1+\alpha)\hat{\ell}/2}^{(1-\alpha)\hat{\ell}/2} \frac{\mathrm{d}z}{\sqrt{z^2 + b^2}} \tag{A1}$$

3. The source point lies at the boundary of two adjacent elements. In this case, $\hat{s}_1$ consists of these two adjacent elements. The last integral in Equation (12) now becomes

$$\frac{q(\mathbf{x})}{4\pi\varepsilon} \int_{-\hat{\ell}_1}^{\hat{\ell}_2} \frac{\mathrm{d}z}{\sqrt{z^2 + b^2}} \tag{A2}$$

   where $\hat{\ell}_1$ and $\hat{\ell}_2$ are the lengths of the elements immediately before and after the source point $\mathbf{x}$ on $\hat{s}_1$.

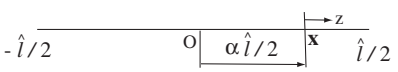

Figure A1. Element $\hat{s}_1$ with source point $\mathbf{x}$.

ACKNOWLEDGEMENTS

This research has been supported by Grant Nos. EEC-0303674 and CMS-0508466 of the National Science Foundation to Cornell University. Sincere thanks are expressed to David Roundy and Hande Üstünel, of the Physics department at Cornell, for their many very useful comments during the course of this research.

REFERENCES

1. Roukes ML. Nanoelectromechanical systems. *Solid-State Sensor and Actuator Workshop*, Hilton Head, SC, 2000.
2. Davis ZJ, Abadal G, Kuhn O, Hansen O, Grey F, Boisen A. Fabrication and characterization of nanoresonating devices for mass detection. *Journal of Vacuum Science Technology B* 2000; **18**:612–616.
3. Boggild P, Hansen TM, Tanasa T, Grey F. Fabrication and actuation of customized nanotweezers with a 25 nm gap. *Nanotechnology* 2001; **12**:331–335.
4. Cleland AL, Roukes ML. Fabrication of high frequency nanometer scale mechanical resonators from bulk Si crystals. *Applied Physics Letters* 1996; **69**:2653–2655.
5. Sazonova V, Yaish Y, Üstünel H, Roundy D, Arias TA, McEuen PL. A tunable carbon nanotube electromechanical oscillator. *Nature* 2004; **431**:284–287.
6. Mukherjee S. *Boundary Element Methods in Creep and Fracture*. Applied Science Publishers: London, 1982.
7. Banerjee PK. *The Boundary Element Methods in Engineering*. McGraw-Hill Europe: Maidenhead, Berkshire, England, 1994.
8. Chandra A, Mukherjee S. *Boundary Element Methods in Manufacturing*. Oxford University Press: New York, 1997.
9. Bonnet M. *Boundary Integral Equation Methods for Solids and Fluids*. Wiley: Chichester, U.K., 1999.
10. Mukherjee S, Mukherjee YX. *Boundary Methods*: *Elements Contours and Nodes*. Taylor and Francis, CRC Press: Bristol, Boca Raton, FL, 2005.
11. Yang TY. *Finite Element Structural Analysis*. Prentice-Hall: New Jersey, 1986.
12. Zienkiewicz OC, Taylor RL. *The Finite Element Method*, vols. 1,2 (4th edn). McGraw-Hill: Maidenhead, Berkshire, U.K., 1994.
13. Hughes TJR. *The Finite Element Method*: *Linear Static and Dynamic Finite Element Analysis*. Dover: Mineola, NY, 2000.
14. Senturia SD, Harris RM, Johnson BP, Kim S, Nabors K, Shulman MA, White JK. A computer-aided design system for microelectromechanical systems (MEMCAD). *Journal of Micro-Electro-Mechanical Systems* 1992; **1**:3–13.
15. Nabors K, White J. FastCap: a multi-pole accelerated 3-D capacitance extraction program. *IEEE Transactions on Computer Aided Design and Integrated Circuits and Systems* 1991; **10**:1447–1459.
16. Gilbert JR, Legtenberg R, Senturia SD. 3D coupled electromechanics for MEMS: applications of CoSolve-EM. *Proceedings of the IEEE* (MEMS) 1995; 122–127.
17. Shi F, Ramesh P, Mukherjee S. Simulation methods for micro-electro-mechanical structures (MEMS) with application to a microtweezer. *Computers and Structures* 1995; **56**:769–783.
18. Aluru NR, White J. An efficient numerical technique for electromechanical simulation of complicated microelectromechanical structures. *Sensors and Actuators A* 1997; **58**:1–11.
19. Mukherjee S, Bao Z, Roman M, Aubry N. Nonlinear mechanics of MEMS plates with a total Lagrangian approach. *Computers and Structures* 2005; **83**:758–768.
20. Shi F, Ramesh P, Mukherjee S. Dynamic analysis of micro-electro-mechanical systems. *International Journal for Numerical Methods in Engineering* 1996; **39**:4119–4139.
21. De SK, Aluru NR. Full-Lagrangian schemes for dynamic analysis of electrostatic MEMS. *Journal of Microelectromechanical Systems* 2004; **13**:737–758.
22. Tang Z, Xu Y, Li G, Aluru NR. Physical models for coupled electromechanical analysis of silicon nanoelectromechanical systems. *Journal of Applied Physics* 2005; **97**:(114304):1–13.
23. Ke C, Espinosa HD. Numerical analysis of nanotube-based NEMS devices—part I: electrostatic charge distribution on multiwalled nanotubes. *Journal of Applied Mechanics* (ASME) 2005; **72**:721–725.
24. Frangi A, di Gioia A. Multipole BEM for the evaluation of damping forces on MEMS. *Computational Mechanics* 2005; **37**:24–31.

25. Harrington RF. *Field Computation by Moment Methods*. IEEE Press: Piscataway, NJ, 1993.
26. Bao Z, Mukherjee S. Electrostatic BEM for MEMS with thin conducting plates and shells. *Engineering Analysis with Boundary Elements* 2004; **28**:1427–1435.
27. Bao Z, Mukherjee S. Electrostatic BEM for MEMS with thin beams. *Communications in Numerical Methods in Engineering* 2005; **21**:297–312.
28. Chuyan SW, Liao YS, Chen JT. Computational study of the effect of finger width and aspect ratios for the electrostatic levitating force of MEMS combdrive. *Journal of Microelectromechanical Systems* 2005; **14**:305–312.
29. Telukunta S, Mukherjee S. Fully Lagrangian modeling of MEMS with thin plates. *Journal of Microelectromechanical Systems* 2006, in press.
30. Mukherjee S, Telukunta S, Mukherjee YX. BEM modeling of damping forces on MEMS with thin plates. *Engineering Analysis with Boundary Elements* 2005; **29**:1000–1007.
31. Liu YJ. Analysis of shell-like structures by the boundary element method based on 3-D elasticity: formulation and verification. *International Journal for Numerical Methods in Engineering* 1998; **41**:541–558.
32. Mukherjee S. On boundary integral equations for cracked and thin bodies. *Mathematics and Mechanics of Solids* 2001; **6**:47–64.
33. Liu YJ, Fan H. On the conventional BIE formulation for piezoelectric solids with defects or of thin shapes. *Engineering Analysis with Boundary Elements* 2001; **25**:77–91.
34. Zhang JM, Tanaka M, Matsumoto T. A simplified approach for heat conduction analysis of CNT-based nano-composites. *Computer Methods in Applied Mechanics and Engineering* 2004; **193**:5597–5609.
35. Nishimura N, Liu YJ. Thermal analysis of carbon nanotube composites using a rigid-line inclusion model by the boundary integral equation method. *Computational Mechanics* 2004; **35**:1–10.
36. Chen JT, Chen KH, Yeih W, Shieh NC. Dual boundary element analysis for cracked bars under torsion. *Engineering Computations* 1998; **15**:732–749.
37. Chen JT, Hong H-K. Review of dual boundary element methods with emphasis on hypersingular integrals and divergent series. *Applied Mechanics Reviews* (ASME) 1999; **52**:17–33.
38. Chandraseker K, Mukherjee S. Coupling of extension and twist in single-walled carbon nanotubes. *Journal of Applied Mechanics* (ASME) 2006, in press.
39. Hayt W, Buck J. *Engineering Electromagnetics* (6th edn). McGraw-Hill: New York, 2001.
40. Nishimura N. Fast multipole accelerated boundary integral equation methods. *Applied Mechanics Reviews* (ASME) 2002; **55**:299–324.
41. Liu YJ, Nishimura N, Otani Y, Takahashi T, Chen XL, Munakata H. A fast boundary element method for the analysis of fiber-reinforced composites based on a rigid-inclusion model. *Journal of Applied Mechanics* (ASME) 2005; **72**:115–128.

